



HAL
open science

Magnetic Field Gradient-Based EKF for Velocity Estimation in Indoor Navigation

Makia Zmitri, Hassen Fourati, Christophe Prieur

► **To cite this version:**

Makia Zmitri, Hassen Fourati, Christophe Prieur. Magnetic Field Gradient-Based EKF for Velocity Estimation in Indoor Navigation. *Sensors*, 2020, 20 (20), pp.1-17. 10.3390/s20205726 . hal-03138331

HAL Id: hal-03138331

<https://hal.science/hal-03138331>

Submitted on 11 Feb 2021

HAL is a multi-disciplinary open access archive for the deposit and dissemination of scientific research documents, whether they are published or not. The documents may come from teaching and research institutions in France or abroad, or from public or private research centers.

L'archive ouverte pluridisciplinaire **HAL**, est destinée au dépôt et à la diffusion de documents scientifiques de niveau recherche, publiés ou non, émanant des établissements d'enseignement et de recherche français ou étrangers, des laboratoires publics ou privés.

Article

Magnetic Field Gradient-Based EKF for Velocity Estimation in Indoor Navigation

Makia Zmitri ¹ , Hassen Fourati ^{1*}  and Christophe Prieur ¹ 

¹ Univ. Grenoble Alpes, CNRS, Grenoble INP, GIPSA-lab, F-38000 Grenoble, France;

* Correspondence: hassen.fourati@gipsa-lab.fr.

Version July 24, 2020 submitted to *Sensors*

Abstract: This paper proposes an advanced solution to improve the inertial velocity estimation of a rigid body, for indoor navigation, through implementing a magnetic field gradient-based Extended Kalman Filter (EKF). The proposed estimation scheme considers a set of data from a triad of inertial sensors (accelerometer and gyroscope), as well as a determined arrangement of magnetometers array. The inputs for the estimation scheme are the spatial derivatives of the magnetic field, from the magnetometers array, and the attitude, from the inertial sensors. As it was shown in the literature, there is a strong relation between the velocity and the measured magnetic field gradient. However, the latter usually suffers from high noises. Then, the novelty of the proposed EKF is to develop a specific equation to describe the dynamics of the magnetic field gradient. This contribution helps to filter, first, the magnetic field and its gradient and second, to better estimate the inertial velocity. Some numerical simulations that are based on an open source database show the targeted improvements. At the end of the paper, this approach is extended to position estimation in the case of a foot-mounted application and the results are very promising.

Keywords: Indoor navigation; magnetic field gradient; spatial derivatives; inertial velocity estimation; Extended Kalman Filter.

1. Introduction

Nowadays, the interest in indoor positioning has been growing exponentially, as it represents a topic of research for many different applications, such as health [1], [2], sports [3], military [4], etc. A wide range of techniques has been investigated to tackle this problem. Some of them require a costly, heavy and pre-installed infrastructure to work (e.g. Wireless Local Area Network (WLAN) [5], Radio Frequency Identification (RFID) [6], etc.). Others rely on more traditional methods such as computer vision techniques [7], which can be inaccessible in certain situations (smoke in building for instance). The most common solution to the case where the conditions of intervention, and the availability of pre-installed equipment are unknown, is the use of low-cost Inertial Measurement Units (IMUs), composed of inertial and magnetic sensors. It represents a promising key to solve many problems in indoor positioning. Usually, the outputs of IMUs are used to calculate the velocity and position through an integration process, or to determine the orientation (attitude) [8] through a specific fusion. Nevertheless, because of sensors biases and noises, these integrations are biased, and then a drift is observed on velocity (integration of linear acceleration) and position (integration of velocity). Numerous techniques have been proposed in the literature to deal with this problem. Some of them depend on a foot-mounted dead reckoning method called Zero-Velocity Update Technique (ZUPT), like in [9] and [10], for example. This method allows to reduce the integration to small steps between phases where the foot is at rest on the ground (stance phase). The drift on velocity and position is thus reduced, especially for the accelerometer measurements integration, which allows a longer use before the system diverges too far away from the actual position. In that process, the better is the velocity,

36 the better is its integration to obtain an improved position. The inertial velocity is also important in
37 other applications, that are not necessarily related to the position estimation. For instance, in [11],
38 drifts in attitude estimation for human and animal motion evaluation are corrected by removing
39 transient accelerations, using a mathematical derivation of velocity measurements coming from a
40 Global Positioning System (GPS) receiver. In the case where GPS measurements are unavailable, or
41 inaccurate, the precision of this proposed approach is degraded. In [12], it is discussed that velocity
42 sensors attached to swimming animals are potentially inaccurate. An evaluation is then conducted
43 with an ellipsoidal micro-turbine that is used to measure the through water speed of a dolphin, by
44 being attached to its body using an array of suction cups. The obtained speed measurements suffer
45 from few drawbacks, such as the inability to track the speed of the disturbed flow when it drops below
46 the turbine stall speed ($U \approx 0.25\text{m/s}$). Other works used the velocity, obtained from a GPS receiver
47 only in the case of outdoor navigation, as an important feature for the classification and prediction of
48 transportation modes [13], [14].

49 1.1. Context

50 The main problem under investigation is the velocity estimation in indoor navigation by means
51 of inertial and magnetic sensors. As known, the presence of magnetic perturbations in indoor
52 environments can be very large [15], due to all metals used in buildings (door frames, aluminum
53 windows, etc.) and potentially to the strong electric currents propagating close-by. Now, one might
54 think that these disturbances can only represent a constraint for indoor positioning. However,
55 these perturbations are not in fact a random noise. On the contrary, they are well structured by
56 physics equations, for instance, Maxwell's equations [16]. The latter represent the propagation of
57 electromagnetic phenomena. Therefore, it is considered that rich information lies in these disturbances.
58 In [17], authors use measurements from an array of 3-axis magnetometers to derive a maximum
59 likelihood estimator. This is in order to determine the displacement of a body through a spatially
60 varying magnetic field. Another recent approach that requires the use of only a 3-axis magnetometer's
61 array, a 3-axis accelerometer and a 3-axis gyroscope, has been firstly introduced in [18], [19]. The
62 proposed technique takes advantage of the magnetic field disturbances, that are observed indoors,
63 to estimate the inertial velocity. This preserves the main advantages of purely inertial technology:
64 no prior mapping or other information are required. Based on this idea, but with different dynamic
65 models, other authors have shown in [20], [21], efficient velocity and position estimation results. In
66 fact, they proved that as long as the magnetic field gradient is non-singular, the velocity is observable
67 and there exists a converging non-linear observer that reconstructs it. In these works, the magnetic
68 field gradient is considered as a measured input for the state-space model and the observer. However,
69 this gradient is usually noisy and is subject to singularities. This influences negatively the observability
70 of the proposed models, which leads to estimation errors. Contrarily, in [19], the authors considered
71 that the magnetic field gradient is not available, instead, the gradient is moved to the state vector and
72 is estimated by an observer. Nevertheless, the gradient's dynamics are modeled by a white noise,
73 which is a questionable choice to the best of authors knowledge, and can influence the estimation of
74 velocity.

75 1.2. Contribution

76 This paper presents a solution to improve the inertial velocity estimation. The proposed approach
77 takes advantage of magnetic disturbances, by using a set of spatially distributed magnetometers to
78 monitor the magnetic field and its spatial derivatives (gradient and its first derivative). The considered
79 state-space model in this work also includes a new magnetic field gradient equation, derived to describe
80 its dynamic. An EKF is proposed to better estimate the inertial velocity in a magnetically disturbed
81 environment, from a 3-axis magnetometer's array, a 3-axis gyroscope and a 3-axis accelerometer. The
82 novelty in the proposed approach is the development of this specific equation to describe the dynamics
83 of magnetic field gradient. This contribution helps better filter the magnetic field and its gradient.

Moreover, it improves the estimation of inertial velocity. The inputs for the estimation scheme are the spatial derivatives of the magnetic field, from the magnetometer's array, and a determined attitude via a gradient descent algorithm, from a triad of inertial and magnetic sensors. A notable improvement on the velocity estimation is shown compared to when the noisy magnetic field gradient is measured and used as an input for the EKF. At the end of the paper, we examine the effect of such velocity improvement on the position estimation in the case of a foot-mounted application aided by ZUPT and the results are very promising.

This paper is organized as follows. In Section 2 some preliminaries and notations are introduced and the principle of magneto-inertial navigation problem is stated, then the magnetic field gradient dynamic equation is established. An EKF is designed in Section 3, where the gradient equation is added, to tackle measurement noises and to estimate not only the velocity but also the magnetic field and its gradient. The EKF is fed with a determined quaternion, given by an attitude estimation block. In Section 4, the ZUPT-aided position estimation is detailed, based on the previous velocity estimation, in the context of foot-mounted inertial navigation. Section 5 presents a scenario test based on an open source database [22] representing a foot-mounted navigation scheme. The obtained results in this case are displayed. While in Section 6, some conclusions and potential future works are stated.

2. Problem formulation

The problem under consideration is how to improve the inertial velocity estimation using only Micro Electro Mechanical Systems (MEMS) inertial sensors, composed of a 3-axis accelerometer and a 3-axis gyroscope, as well as a spatially distributed 3-axis magnetometer's array. A new state-space model is proposed and its contribution is demonstrated through an EKF-based approach. In the end of the paper, the obtained results of the improved velocity estimation are extended to the position estimation in a foot-mounted framework.

2.1. Notation

To address the problem cited above, two frames are used:

- a local inertial frame \mathfrak{R}_n fixed to the Earth and its associated orthonormal basis $\mathfrak{B}_n = (\vec{i}_n, \vec{j}_n, \vec{k}_n)$;
- a body frame \mathfrak{R}_b attached to the moving rigid body and its associated orthonormal basis $\mathfrak{B}_b = (\vec{i}_b, \vec{j}_b, \vec{k}_b)$.

Variables expressed in \mathfrak{R}_n (resp. \mathfrak{R}_b) are marked by the subscript n (resp. b).

Let $R_{b \leftarrow n} \in SO(3)$ be the rotation matrix between the two frames, from \mathfrak{R}_n to \mathfrak{R}_b . For the sake of simplicity, in the rest of the paper the notation $R_{b \leftarrow n}$ is omitted and is replaced by R . This matrix can be expressed in terms of quaternion as follows

$$R = \begin{bmatrix} 2(q_0^2 + q_1^2) - 1 & 2(q_1q_2 + q_0q_3) & 2(q_1q_3 - q_0q_2) \\ 2(q_1q_2 - q_0q_3) & 2(q_0^2 + q_2^2) - 1 & 2(q_0q_1 + q_2q_3) \\ 2(q_0q_2 + q_1q_3) & 2(q_2q_3 - q_0q_1) & 2(q_0^2 + q_3^2) - 1 \end{bmatrix} \quad (1)$$

The unit quaternion, denoted by q , is a hypercomplex number of rank 4 such that,

$$q = [q_0 \ q_{vect}^\top]^\top \quad (2)$$

where q_0 is the scalar part and $q_{vect} = [q_1 \ q_2 \ q_3]^\top$ is the vector part of quaternion. The reader is invited to refer to [23] for more details about quaternion algebra.

The rigid body under consideration can simultaneously translate and rotate in 3D space, and its displacement is represented with the position vector $M_n = [x_n \ y_n \ z_n]^\top \in \mathbb{R}^{3 \times 1}$ in \mathfrak{R}_n . Then $v_n = \frac{dM_n}{dt} = [v_{nx} \ v_{ny} \ v_{nz}]^\top \in \mathbb{R}^{3 \times 1}$ the inertial velocity vector, to be estimated in \mathfrak{R}_n , and $a_n = \frac{dv_n}{dt} = [a_{nx} \ a_{ny} \ a_{nz}]^\top \in \mathbb{R}^{3 \times 1}$ the acceleration vector. Vectors v_n and a_n can also be expressed in \mathfrak{R}_b by simply multiplying them by R .

119 Since inertial and magnetic sensors are used in this framework, then the following variables are
120 considered:

- The angular velocity $\omega^{\frac{b}{n}} = [\omega_x \ \omega_y \ \omega_z]^\top \in \mathbb{R}^{3 \times 1}$, of \mathfrak{R}_b with respect to \mathfrak{R}_n , measured by a 3-axis gyroscope. The corresponding skew-symmetric matrix is defined such as

$$[\omega^{\frac{b}{n}} \times] = \begin{pmatrix} 0 & -\omega_z & \omega_y \\ \omega_z & 0 & -\omega_x \\ -\omega_y & \omega_x & 0 \end{pmatrix} \quad (3)$$

- 121 • The acceleration $a_b = [a_{bx} \ a_{by} \ a_{bz}]^\top \in \mathbb{R}^{3 \times 1}$ of \mathfrak{R}_b , measured by a 3-axis accelerometer;
- 122 • The magnetic field $B_b = [B_{bx} \ B_{by} \ B_{bz}]^\top \in \mathbb{R}^{3 \times 1}$, measured in \mathfrak{R}_b by a 3-axis magnetometer,
123 which depends on time and space;
- 124 • The Jacobian matrix $\nabla B_b \in \mathbb{R}^{3 \times 3}$, which represents the magnetic field gradient, measured on a
125 fixed point $P_b = [x_{bp} \ y_{bp} \ z_{bp}]^\top \in \mathbb{R}^{3 \times 1}$ and defined by

$$\nabla B_b(P_b(t)) = \frac{\partial B_b(P_b(t))}{\partial P_b(t)} \quad (4)$$

126 2.2. Magnetic field and its gradient

A rigid body located inside a magnetically disturbed area is considered, which is a situation that is often observed indoors [15]. The disturbances on the magnetic field are useful information in this work. According to Maxwell's equations [16], the dynamic of the magnetic field measured in \mathfrak{R}_b obeys to the following equation¹

$$\frac{dB_b}{dt} = -\omega^{\frac{b}{n}} \times B_b + \nabla B_b v_b \quad (5)$$

This equation ensures that v_b is observable and can be estimated, provided that ∇B_b is non-singular (see [18] for observability proof). Under this assumption, the velocity can be estimated using ∇B_b , which enhances the performance of any inertial navigation system, as it has been demonstrated in [19]. However, one of the major remaining difficulties, is to reliably measure ∇B_b . For this purpose, a spatially distributed magnetometer's array is considered. This array provides magnetic field measurements that are usually noisy, then, when computing spatial derivatives, this noise can get larger. It follows that ∇B_b is also corrupted by noise. This noise can degrade the velocity estimation especially when ∇B_b has low values (more precise simulations on the matter are in [20]). A way to tackle this problem is to filter ∇B_b . To do so, an equation representing its dynamic should be proposed. For that, the temporal derivative of ∇B_n in \mathfrak{R}_n is introduced such as,

$$\frac{d\nabla B_n}{dt} = \frac{d\nabla B_n}{dM_n} \frac{dM_n}{dt} = T_n v_n \quad (6)$$

where $T_n \in \mathbb{R}^{3 \times 3 \times 3}$ is a tensor representing the first spatial derivative of ∇B_n in \mathfrak{R}_n and can be represented as follows:

$$T_n = \frac{d\nabla B_n}{dM_n} = \begin{bmatrix} \nabla \alpha_{11} & \nabla \alpha_{12} & \nabla \alpha_{13} \\ \nabla \alpha_{21} & \nabla \alpha_{22} & \nabla \alpha_{23} \\ \nabla \alpha_{31} & \nabla \alpha_{32} & \nabla \alpha_{33} \end{bmatrix} \quad (7)$$

and $\nabla \alpha_{ij} = [\frac{\partial \alpha_{ij}}{\partial x_m} \ \frac{\partial \alpha_{ij}}{\partial y_m} \ \frac{\partial \alpha_{ij}}{\partial z_m}]_{1 \leq i,j \leq 3}$, with α_{ij} representing the elements of ∇B_n .

¹ \times is the cross product of two vectors in \mathbb{R}^3 .

The temporal derivative $\frac{d\nabla B_n}{dt}$ can also be written such as

$$\begin{aligned} \frac{d\nabla B_n}{dt} &= \frac{d(R^\top \nabla B_b R)}{dt} = \frac{dR^\top}{dt} \nabla B_b R + R^\top \frac{d\nabla B_b}{dt} R + R^\top \nabla B_b \frac{dR}{dt} \\ &= R^\top [\omega_n^b \times] \nabla B_b R + R^\top \frac{d\nabla B_b}{dt} R + R^\top \nabla B_b (-[\omega_n^b \times] R) \end{aligned} \quad (8)$$

From (6) and (8) the following equality is obtained

$$R^\top \frac{d\nabla B_b}{dt} R = T_n v_n + R^\top \nabla B_b [\omega_n^b \times] R - R^\top [\omega_n^b \times] \nabla B_b R \quad (9)$$

By multiplying both sides of (9) by R and R^\top respectively, the following equation is deduced,

$$\frac{d\nabla B_b}{dt} = T_b v_b + \nabla B_b [\omega_n^b \times] - [\omega_n^b \times] \nabla B_b \quad (10)$$

127 where T_b is the first spatial derivative of ∇B_b , with the same form as (7), represented in \mathfrak{R}_b . The reader
128 can check [24] for more information on how T_b is measured.

129 In Section 3, the dynamic model, specific to the studied problem, is expanded by including (10), and
130 an EKF is designed to filter ∇B_b to improve the velocity estimation.

131 3. Inertial velocity, magnetic field and magnetic field gradient estimation

132 This section is focused mainly on the inertial velocity estimation, by using an IMU and an array
133 of spatially distributed magnetometers. A block diagram of the proposed approach is shown in Fig. 1.
134 The main novelty resides on the blue block, which represents a magnetic field gradient-based EKF
135 for estimating not only the inertial velocity \widehat{v}_n , but also the magnetic field \widehat{B}_b , and its gradient $\widehat{\nabla B}_b$.
136 This EKF is fed with an estimated quaternion \widehat{q} , given by the green block, that depicts a gradient
137 descent attitude estimation algorithm [25]. The two blocks are explained in details in the following
sub-sections.

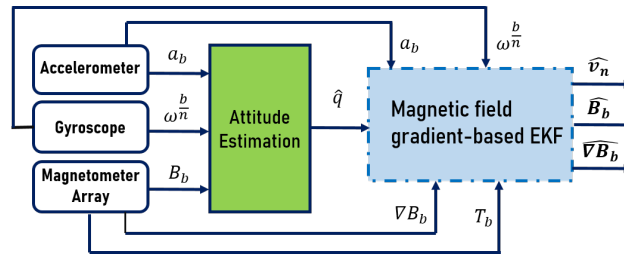


Figure 1. Overall diagram for estimation

138

139 3.1. Magnetic field gradient-based EKF

A magnetic field gradient-based EKF is proposed based on a 3-axis magnetometer's array, a 3-axis gyroscope and a 3-axis accelerometer. The continuous-time dynamic model used to establish the EKF can be written such as

$$\begin{cases} \frac{dv_n}{dt} = R(\widehat{q})^\top a_b - g \\ \frac{dB_b}{dt} = -\omega_n^b \times B_b + \nabla B_b R(\widehat{q}) v_n \\ \frac{d\nabla B_b}{dt} = T_b R(\widehat{q}) v_n + \nabla B_b [\omega_n^b \times] - [\omega_n^b \times] \nabla B_b \end{cases} \quad (11)$$

The state vector for this dynamic state-space model is $x = [v_n \ B_b \ \nabla B_b]^\top \in \mathbb{R}^{11 \times 1}$, the input vector is $u = [\hat{q} \ \omega_n^b \ a_b \ T_b]^\top \in \mathbb{R}^{17 \times 1}$, and the output (measurement) vector is $y = [B_b \ \nabla B_b]^\top \in \mathbb{R}^{8 \times 1}$. Recall that 7 elements of T_b are sufficient to calculate all the tensor's components [24]. The matrix $R(\hat{q})$ is defined in (1), where \hat{q} is the estimated quaternion. Note that the term v_b in (5) and (10) is replaced by $R(\hat{q})v_n$ since the inertial velocity needs to be estimated in \mathfrak{R}_n rather than in \mathfrak{R}_b .

The magnetic field measurements are usually noisy, then, when extracting higher order derivatives (in this case ∇B_b), this noise can get more important, due to the different approximations taken into account in some numerical computations. It follows that ∇B_b is also affected by noise. This can cause unbounded velocity estimation errors especially when ∇B_b has low values (more precise simulations on the matter are in [20]). For this reason, filtering ∇B_b instead of using it directly as an input, corrupted with noise, in the EKF, improves the velocity estimation. As T_b , defined in (10), is measurable, it is possible to add ∇B_b to x . A first schema of the magnetic field gradient-based EKF was presented in [24]. The estimation approach was based on two EKFs, in cascade, as displayed in Fig. 2. The primary EKF used the third equation in (11) as a dynamic model while the main EKF used the first and second equations in (11).

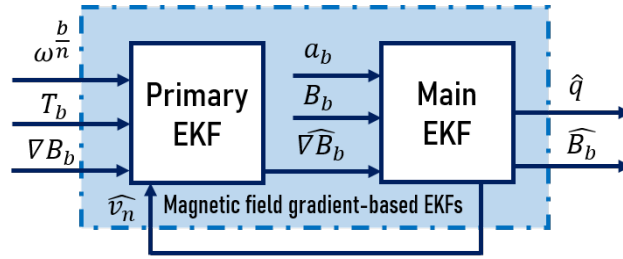


Figure 2. Magnetic field gradient-based EKFs [24]

To go further in this paper, we propose to simplify the estimation architecture in Fig. 2, by using the compact dynamic model (11). The general schema of estimation is presented in Fig. 3, where a single EKF is rather used.

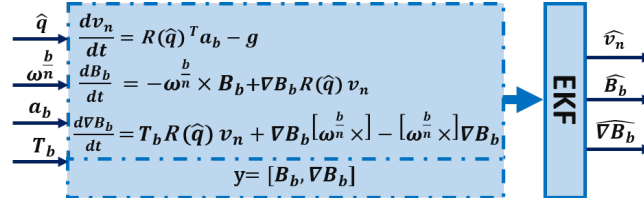


Figure 3. Magnetic field gradient-based EKF

The two models for process and measurements in Fig. 3 can be represented by the following general nonlinear form:

$$\begin{aligned} x[k] &= f(x[k-1], u[k], v[k]) \\ y[k] &= h(x[k], u[k], \eta[k]) \end{aligned} \quad (12)$$

140 where $x[k]$ is the state vector at time step k , $y[k]$ is the measurement vector, $u[k]$ is the input, $f(\cdot)$ is a
 141 nonlinear function that represents the state-space model, $h(\cdot)$ is a nonlinear function that represents
 142 the measurement model, and $v[k]$ and $\eta[k]$ are the process and measurement noises, respectively, and
 143 are assumed to be zero-mean, white, Gaussian and uncorrelated. Note that in order to determine
 144 $f(\cdot)$ and $h(\cdot)$, a discretization procedure that transforms the continuous-time equations in Fig. 3 into
 145 a discrete-time model must be undertaken. The Runge-Kutta 4th order method [26] is used for the
 146 discretization.

147 3.2. Quaternion estimation

The kinematic equation describing the variation of rigid body's attitude in term of quaternion, can be defined from angular velocity measurements given by a 3-axis gyroscope such as,

$$\frac{dq}{dt} = \frac{1}{2}[\omega_q \times]q = \frac{1}{2} \begin{pmatrix} 0 & -\omega_x & -\omega_y & -\omega_z \\ \omega_x & 0 & \omega_z & -\omega_y \\ \omega_y & -\omega_z & 0 & \omega_x \\ \omega_z & \omega_y & -\omega_x & 0 \end{pmatrix} q \quad (13)$$

148 where $\omega_q = [0 \ \omega_n^b]^\top \in \mathbb{R}^{4 \times 1}$, the quaternion form of angular velocity, and $[\omega_q \times]$ is its
 149 skew-symmetric matrix. However, the gyroscope has a long-term drift which is due to noise and
 150 bias. So, by simply integrating (13), a drift can be observed on quaternion. The most common
 151 solution for such problem is to use a data fusion approach that merges measurements coming from
 152 gyroscopes, accelerometers, and magnetometers. The main methods are based on Kalman filters
 153 (KFs) [27], Extended Kalman filters (EKFs) [28], complementary filters [29], [25], [30], or observers [31].
 154 Nevertheless, one should keep in mind the problem of magnetic disturbances in indoor navigation.
 155 These perturbations are known to affect the precision of most attitude determination techniques, which
 156 calls for approaches that investigate this case, such as in [28], [31] and [25].

157 In [25], authors proposed a new algorithm that uses inertial and magnetic measurements to
 158 provide a precise attitude estimation through incorporating magnetic distortion and gyroscope
 159 drift compensations. The main idea is to use a 3-axis accelerometer and a 3-axis magnetometer
 160 measurements in an analytically derived and optimized gradient descent algorithm, in order to
 161 compute the direction of gyroscope measurement error as a quaternion derivative. This algorithm
 162 is computationally inexpensive, as it requires 277 scalar arithmetic operations each update step, it
 163 is efficient at low sampling rates and it has only two adjustable parameters defined by observable
 164 system characteristics. Moreover, it eliminates the need for the reference direction of Earth's magnetic
 165 field to be predefined. Then, in what follows, this algorithm is implemented (green block in Fig. 1) to
 166 determine \hat{q} .

167 4. Position estimation in the context of foot-mounted inertial navigation

168 In this section, we examine the effect of such velocity estimation improvement on the position
 169 one, with a focus on a foot-mounted navigation framework. The proposed algorithm is a combination
 170 between the magnetic field gradient-based EKF and ZUPT. The general schema of estimation is
 171 presented in Fig. 4. The right red block represents the zero-velocity detector, denoted d . In the case
 172 where $d = 1$, a zero-velocity update (left red block) is applied on the estimated inertial velocity \widehat{v}_n
 173 resulting from the blue block. The updated velocity \widehat{v}_{nZupt} is fed to the yellow block for integration, in
 174 order to obtain the position \widehat{M}_n . The red blocks are described in the following subsections.

175 4.1. Zero-velocity detector

The objective of a zero-velocity detector is to decide whether, during a time epoch that consists of $W \in \mathbb{N}$ observations (i.e. window size) between the time instants l and $l + W - 1$, the IMU is moving or stationary, given the measurements a_b and ω_n^b . At each sample, this detector, denoted d , can have one of the two values: $d = 1$, which corresponds to the stance phase (the entire period during which the foot is on the ground) or $d = 0$, which represents the swing phase (the entire period during which the foot is in the air for limb advancement). Mathematically, this detection process can be seen as a binary hypothesis testing problem, where the detector indicates that the IMU is stationary (i.e. $d = 1$) if,

$$T_s(a_b, \omega_n^b) \leq \gamma \quad (14)$$

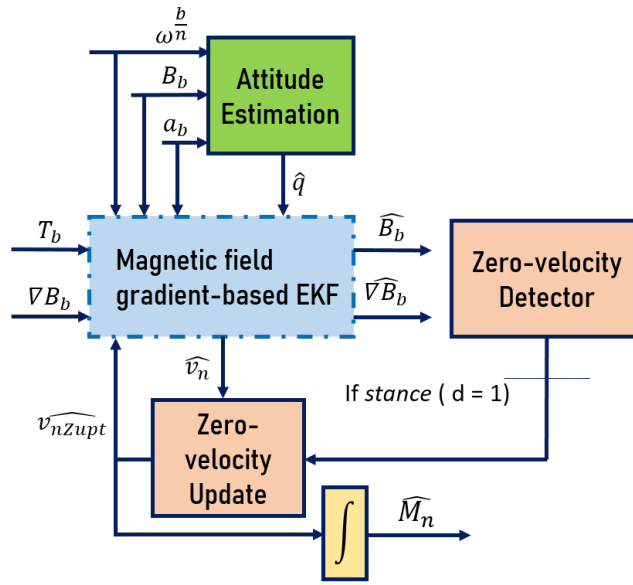


Figure 4. ZUPT-aided position estimation

with $T_s(a_b, \omega_n^b)$, the test statistics of the detector and γ , the detection threshold.

The test statistics can have multiple forms depending on the chosen detector. In related works, different detectors have been evaluated [10] from the ones depending only on accelerometer data (such as Acceleration Moving Variance Detector and Acceleration Magnitude Detector), to those that are angular rate-based (Angular Rate Energy Detector), or even pressure measurements [32]. In this paper, the Stance Hypothesis Optimal Detector (SHOE) [33] is chosen, as it represents a combination between acceleration and angular rate-based detectors, and has proven to outperform other detectors in the literature for its robustness to changes in gait speed as well as its high positional accuracy. Concretely, SHOE computes $T_s(a_b, \omega_n^b)$ in the following way,

$$T_s(a_b, \omega_n^b) = \frac{1}{W} \sum_{k=l}^{l+W-1} \left(\frac{1}{\sigma_a^2} \|a_{b,k} - g \frac{\bar{a}_{b,l}}{\|\bar{a}_{b,l}\|}\|^2 + \frac{1}{\sigma_\omega^2} \|\omega_k^b\|^2 \right) \quad (15)$$

176 where W is the window size (the number of sensor readings), $\sigma_a^2, \sigma_\omega^2$ are the variances of the acceleration
 177 and angular rate measurements, $\bar{a}_{b,l}$ denotes the mean over W samples, and g is the gravity.

178 4.2. ZUPT

179 If the detector d has declared the stationary case (i.e. $d = 1$), \hat{v}_n should give a zero-velocity
 180 estimate. However, due to diverse errors, it most likely will not. This motivates the use of ZUPT, as it
 181 corrects these drifts, which greatly improves the velocity estimation, as it was shown in the literature. If
 182 $d = 1$ at time k , the actual value of inertial velocity is assumed to be known, and then its estimate \hat{v}_n
 183 is reset to zero. This is actually done inside the EKF, in a way where the velocity estimate \hat{v}_n is constantly
 184 corrected. In Fig. 4, the ZUPT-based velocity estimate is represented with \widehat{v}_{nZupt} . Consequently, by
 185 updating the velocity estimate, a better position estimation should be obtained after integrating \widehat{v}_{nZupt}
 186 (yellow box in Fig. 4).

187 5. Simulations and results

188 In this section, the performance of the proposed magnetic field gradient-based EKF is displayed.
 189 The improvements on inertial velocity estimation are highlighted when ∇B_b is filtered. In the end,
 190 we examine the effect of such improvement on the position in a foot-mounted navigation framework
 191 aided by ZUPT.

192 5.1. Groundwork for simulations

193 One of the most common problems in pedestrian navigation, is the knowledge of ground truth,
 194 as it enables to compare proposed algorithms and contributions with references. In [22], authors
 195 simulate a trajectory (position and attitude), that is based on a real human walk pattern. A synthetic
 196 noiseless IMU data is provided. A set of signals from a spatially distributed magnetometers array is
 197 also considered (one signal is given by [22] and the others are simulated accordingly). The reader can
 198 refer to this website: <https://lopsi.weebly.com/downloads.html>, to download one of the proposed
 199 data sets corresponding to ground truth trajectories, and to have more details about the different
 200 chosen parameters. In this simulation, a closed 3-loop trajectory in rectangular path of $12 \times 7m$ is used
 201 to represent the ground truth. Then, an additive random zero-mean white Gaussian noise is added as
 detailed in Table 1.

Table 1. Standard deviations of considered noises from datasheet of MTi module (Xsens) [34]

	Noise standard deviation
Accelerometer [ms^{-2}]	0.012
Gyroscope [$rads^{-1}$]	0.0087
Magnetometers [G]	0.03

202

203 5.2. Main results

204 5.2.1. Attitude estimation results

205 To determine the body attitude in quaternion, Madgwick's gradient descent algorithm [25] is
 206 used, as it has been proven robust to magnetic disturbances. The constant $\beta = 0.008$ (divergence
 207 rate) is fixed through a trial and error scheme and by taking into account gyroscope measurements
 208 error. The estimated quaternion \hat{q} is used to calculate the rotation matrix $R(\hat{q})$ through (1). This matrix
 209 is important in velocity estimation as it is used in the model in Fig. 3. The estimated quaternion is
 converted into Euler angles as shown in Fig. 5.

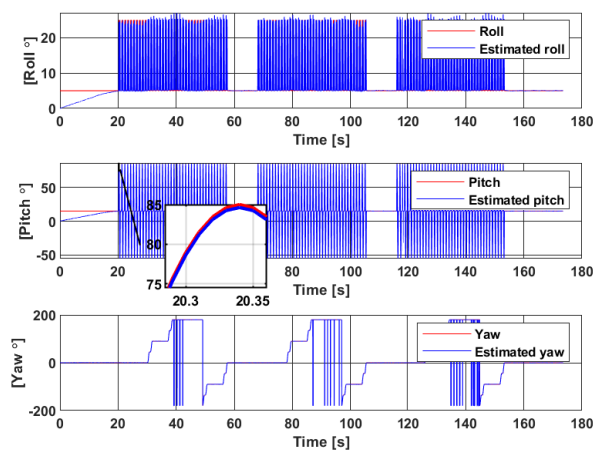


Figure 5. Euler angles estimation through Madgwick filter [25]

210

211 The estimated Euler angles converge in less than 20s despite initializing the EKF with values that are
 212 different from the true ones. Moreover, the filter is robust against the high standard deviation noise
 213 added to magnetic measurements. However, some jumps are seen on the *yaw* estimation when the

214 angle reaches 180° , which is explained by the fact that quaternion cannot represent a rotation exceeding
 215 180° in any direction. This affects position reconstruction along the z -axis.

216 5.2.2. Magnetic field gradient-based EKF results

217 As proposed earlier in this paper, ∇B_b should be filtered from noise, in the purpose of better
 218 estimating the inertial velocity. Fig. 6 displays the estimation results for the first element α_{11} of ∇B_b .
 219 The estimated gradient (in blue dashed line) is close to the theoretical one (in red solid line) even
 though the initialization values are different from the ground-truth ones.

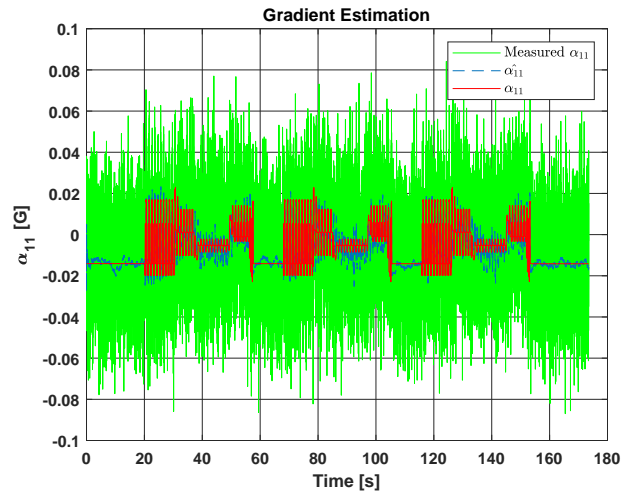


Figure 6. Estimation of the first element α_{11} of ∇B_b

220 Let $\eta_{\alpha_{11}}$ represent the noise of the first element α_{11} of ∇B_b . In Fig. 7, the Power Spectral Density
 221 (PSD) [35] of this noise is presented, before and after filtering ∇B_b with the proposed EKF. This metric
 222 represents the square of Fourier transformation module, divided by the spectral bandwidth. It basically
 223 describes how the power of a signal is distributed over frequency, which is an interesting criterion to
 224 evaluate the noise compensation.

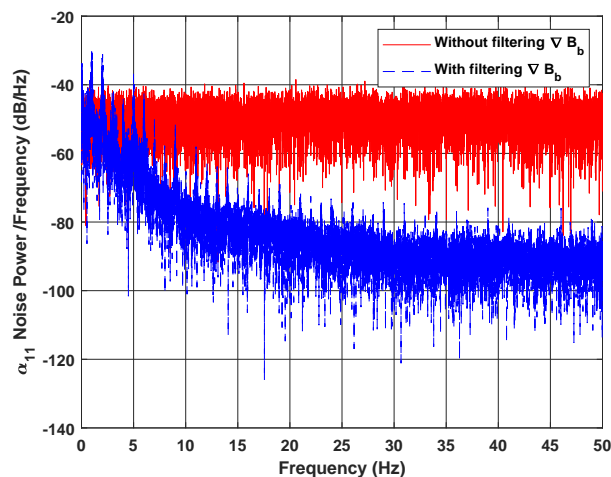


Figure 7. α_{11} noise PSD with and without filtering ∇B_b

225 Fig. 7 shows that in case ∇B_b is filtered (by adding (10) to (11)), the noise power of its elements
 226 (e.g. α_{11} in this case), represented in blue dashed line, is inferior than the one of when the filtering
 227 process is not applied (when ∇B_b is not in the state vector), represented in red solid line, and it
 228 decreases continuously along the frequency range. The mean of noise PSD error between both cases is
 229

around ≈ -29.77 dB, which justifies the effectiveness of the proposed approach. Another way that is used to quantify noise in a signal is by computing the Signal to Noise Ratio (SNR) [35], which is the ratio of the power of true signal α_{11} to the power of its noise $\eta_{\alpha_{11}}$. The SNR of α_{11} increases from $SNR_{without} = -9.46$ dB when ∇B_b is not filtered, to $SNR_{with} = -0.42$ dB, when it is done. This proves again that ∇B_b noise is greatly reduced with the proposed model and filter. The advantage of this filtering process is also observed during the velocity estimation, as shown in Fig. 8, where the x axis component of the inertial velocity is plotted. The velocity estimate \widehat{v}_{nx} (green solid line) given by the proposed approach is closer to the ground truth velocity (red solid line) than when ∇B_b is used as a noisy input (blue solid line).

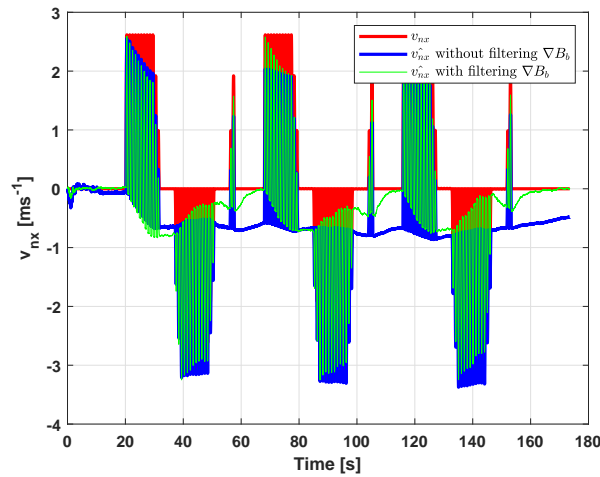


Figure 8. Estimation of v_{nx} with and without filtering ∇B_b

As indicated in Table 2, the RMSE between the estimated velocity \widehat{v}_n and the true one v_n is 0.37 ms^{-1} for the case where the proposed approach is not applied, versus 0.27 ms^{-1} when it is done. This improvement is beneficial in some applications that require measuring the velocity with a certain precision. The performance of the magnetic field gradient-based EKF is also compared to the first work [24] and better results are shown in terms of velocity RMSE. This improvement is obtained thanks to the better tuning of the state and measurement noise covariance matrices of the proposed EKF. From Table 2, it can be seen that the main contribution of this work resides on the yellow colored line, where the smallest value of RMSE compared to the other approaches is observed.

Table 2. RMSE of the velocity estimation

	v_n RMSE [ms^{-1}]
Without filtering ∇B_b	0.37
With filtering ∇B_b in a primary EKF [24]	0.29
With filtering ∇B_b	0.27

246

247 5.2.3. Application: Extending to position estimation

248 One possible application that highlights the importance of the decrease on the velocity estimation
 249 error, is the position reconstruction through an integration of \widehat{v}_n (without ZUPT). The impact can be
 250 seen by plotting the 2D representation of the estimated trajectory. A noticeable drift compensation is
 251 observed when ∇B_b is filtered. Indeed, the slightest improvement in velocity estimation can largely
 252 affect the reconstruction of trajectory, as less errors are generated, and thus less of their accumulation
 253 during the integration process. Table 3 presents the RMSE between the estimated position and the
 254 ground truth for the three studied approaches. As the case for velocity, the best results are achieved

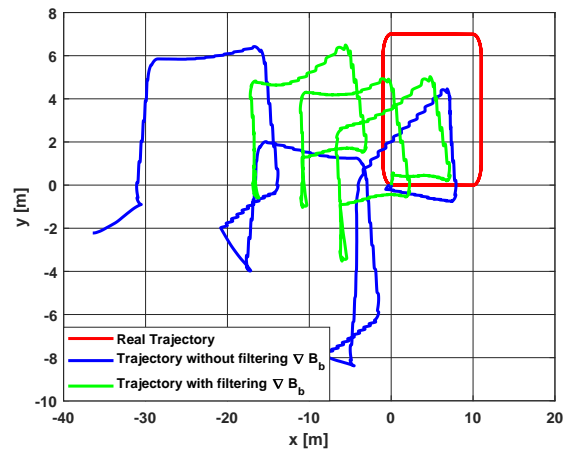


Figure 9. 2D trajectory reconstruction with and without filtering ∇B_b

255 when ∇B_b is filtered with the proposed EKF. This is clearly expected as the position is obtained from
 256 integrating the estimated velocity \widehat{v}_n .

Table 3. RMSE of the position estimation

	M_n RMSE [m]
Without filtering ∇B_b	31.60
With filtering ∇B_b in a primary EKF [24]	25.18
With filtering ∇B_b	20.88

256
 257 Now despite the previously mentioned contribution in inertial velocity estimation, the obtained error
 258 results are still considered high if position reconstruction needs to be done, which is observed in
 259 Table 3. In fact, whether its computed with or without the proposed model, \widehat{v}_n still suffers from some
 260 errors, which are due to the different uncertainties considered in the simulation scenario, i.e. the
 261 approximations taken into account to extract the spatial derivatives (T_b for instance), the linearization
 262 process of the EKF, the tuning of the process and measurements covariances, etc. These errors lead
 263 to drifts if position needs to be reconstructed, which is seen in Fig. 9. Note also that a noise with a
 264 large standard deviation is applied on magnetometers measurements, in order to better highlight
 265 the contribution of filtering ∇B_b . Nevertheless, better velocity estimation results can be obtained
 266 in case the values of the different noises are lowered, which improves consequently the position
 267 reconstruction.

268 5.2.4. Zero-velocity update results

269 For the different reasons stated above, the proposed magnetic field gradient-based EKF
 270 combined with ZUPT (the red blocks in Fig. 4), and the same comparisons are done on the position
 271 reconstruction as the ones in Fig. 9. The pertinence of this approach on the velocity estimation in the
 272 case of foot-mounted applications is discussed in Section 4. By correcting the velocity estimate \widehat{v}_n
 273 with ZUPT, better position estimation results are obtained, and drifts on all 3-axis are almost entirely
 274 removed. In fact, Fig. 10 shows that even when adding ZUPT, the proposed approach (with filtering
 275 ∇B_b), still outperforms the case of when the filtering is not applied (use ∇B_b as a noisy input). Note
 276 that the starting and arrival points for the ground truth trajectory are the same (red dot). It is observed
 277 that the arrival point of the green plot is closer to the ground truth one than the blue plot, which
 278 highlights the contribution of filtering ∇B_b . It can also be seen from the points coordinates that the
 279 drift on the z axis is greatly reduced in the case of filtering ∇B_b . In Table 4, a comparison between
 280 position RMSEs is displayed when ZUPT is added, which shows how the latter is reduced when ∇B_b

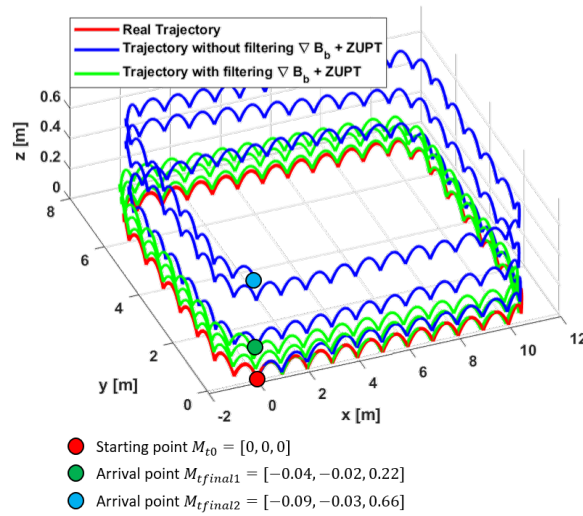


Figure 10. Trajectory reconstruction aided by ZUPT with and without filtering ∇B_b

281 is filtered. The obtained distance error with the proposed EKF after adding ZUPT also decreases from
 282 1.22% of the total traveled distance to 0.41% with the proposed approach, which proves again the
 importance of filtering ∇B_b .

Table 4. Results of ZUPT-aided position estimation

	M_n RMSE [m]	Distance error [%]
Without filtering $\nabla B_b + ZUPT$	0.26	1.22
Filtering ∇B_b in a primary EKF+ZUPT	0.14	0.88
With filtering $\nabla B_b + ZUPT$	0.11	0.41

283

284 6. Conclusion and future work

285 In this paper, the inertial velocity estimation was improved using a magnetic field gradient-based
 286 EKF. This was done by reducing noise from the magnetic field gradient, thanks to a newly introduced
 287 equation that better describes its dynamic. The proposed approach was then combined with ZUPT in
 288 order to estimate position in a foot-mounted application. Applying this approach on real experimental
 289 data is definitely the next step. Tuning the EKF covariance matrices with artificial intelligence-based
 290 approaches is also a topic that will be considered in future works.

291 **Author Contributions:** M.Z., currently a PhD student at GIPSA-Lab, has achieved this work with the collaboration
 292 of her supervisors, H.F., associate professor at the University Grenoble Alpes, and C.P., CNRS Senior Researcher.
 293 The conceptualization, methodology and programming of this work were conducted by M.Z., the investigation
 294 and analysis of the different results were elaborated with the help of H.F. and C.P. The original draft preparation
 295 was done by M.Z., followed by corrections and refinements from H.F. and C.P. All authors have read and agreed
 296 to the published version of the manuscript.

297 **Acknowledgments:** This work has been partially supported by MIAI@Grenoble Alpes, (ANR-19-P3IA-0003).

298 **Conflicts of Interest:** The authors declare no conflict of interest.

299 References

- 300 1. Draghici, I.; Vasileteanu, A.; Goga, N.; Pavaloiu, B.; Guta, L.; Mihailescu, M.N.; Boiangiu, C. Indoor
 301 positioning system for location based healthcare using trilateration with corrections. International
 302 Conference on Engineering, Technology and Innovation (ICE/ITMC); , 2017; pp. 169–172.

- 303 2. Van Haute, T.; De Poorter, E.; Crombez, P.; Lemic, F.; Handziski, V.; Wirstrom, N.; Wolisz, A.; Voigt, T.;
304 Moerman, I. Performance analysis of multiple Indoor Positioning Systems in a healthcare environment.
305 *International Journal of Health Geographics* **2016**, *15*, 7.
- 306 3. Ridolfi, M.; Vandermeeren, S.; Defraye, J.; Steendam, H.; Gerlo, J.; Clercq, D.; Hoebeke, J.; De Poorter, E.
307 Experimental Evaluation of UWB Indoor Positioning for Sport Postures. *Sensors* **2018**, *18*, 168.
- 308 4. Rantakokko, J.; Rydell, J.; Strömbäck, P.; Händel, P.; Callmer, J.; Tornqvist, D.; Gustafsson, F.; Jobs, M.;
309 Grudén, M. Accurate and reliable soldier and first responder indoor positioning: Multisensor systems and
310 cooperative localization. *IEEE Wireless Communications* **2011**, *18*, 10–18.
- 311 5. Duan, Y.; Lam, K.; Lee, V.C.S.; Nie, W.; Liu, K.; Li, H.; Xue, C.J. Data Rate Fingerprinting: A WLAN-Based
312 Indoor Positioning Technique for Passive Localization. *IEEE Sensors Journal* **2019**, *19*, 6517–6529.
- 313 6. Xu, H.; Wu, M.; Li, P.; Zhu, F.; Wang, R. An RFID Indoor Positioning Algorithm Based on Support Vector
314 Regression. *Sensors* **2018**, *18*, 1504.
- 315 7. Martín-Gorostiza, E.; García-Garrido, M.-A. and Pizarro, D.; Salido-Monzú, D.; Torres, P. An Indoor
316 Positioning Approach Based on Fusion of Cameras and Infrared Sensors. *Sensors* **2019**, *19*, 2519.
- 317 8. Michel, T.; Genevès, P.; Fourati, H.; Layaïda, N. Attitude estimation for indoor navigation and augmented
318 reality with smartphones. *Pervasive and Mobile Computing* **2018**, *46*, 96–121.
- 319 9. Fourati, H. Heterogeneous data fusion algorithm for pedestrian navigation via foot-mounted inertial
320 measurement unit and complementary filter. *IEEE Transactions on Instrumentation and Measurement* **2015**,
321 *64*, 221–229.
- 322 10. Skog, I.; Nilsson, J.O.; Händel, P. Evaluation of zero-velocity detectors for foot-mounted inertial navigation
323 systems. International Conference on Indoor Positioning and Indoor Navigation (IPIN); , 2010; pp. 1–6.
- 324 11. Fourati, H.; Manamanni, N.; Afilal, L.; Handrich, Y. A Nonlinear Filtering Approach for the Attitude and
325 Dynamic Body Acceleration Estimation Based on Inertial and Magnetic Sensors: Bio-Logging Application.
326 *IEEE Sensors Journal* **2011**, *11*, 233–244.
- 327 12. Gabaldon, J.; Turner, E.; Johnson-Roberson, M.; Barton, K.; Johnson, M.; Anderson, E.; Shorter, K.
328 Integration, Calibration, and Experimental Verification of a Speed Sensor for Swimming Animals. *IEEE*
329 *Sensors Journal* **2019**, *19*, 3616–3625.
- 330 13. Erdelić, M.; Carić, T.; Ivanjko, E.; Jelušić, N. Classification of Travel Modes Using Streaming GNSS Data.
331 *Transportation Research Procedia* **2019**, *40*, 209–216.
- 332 14. Yang, X.; Stewart, K.; Tang, L.; Xie, Z.; Li, Q. A Review of GPS Trajectories Classification Based on
333 Transportation Mode. *Sensors* **2018**, *18*, 3741.
- 334 15. Bachmann, E.R.; Yun, X.; Peterson, C.W. An investigation of the effects of magnetic variations on
335 inertial/magnetic orientation sensors. International Conference on Robotics and Automation; , 2004; pp.
336 1115–1122.
- 337 16. Jackson, J. *Classical Electrodynamics*; Third Edition. John Wiley & Sons, Inc., 1998.
- 338 17. Skog, I.; Hendeby, G.; Gustafsson, F. Magnetic Odometry - A Model-Based Approach Using a Sensor Array.
339 International Conference on Information Fusion (FUSION); , 2018; pp. 794–798.
- 340 18. Vissière, D.; Martin, A.; Petit, N. Using spatially distributed magnetometers to increase IMU-based velocity
341 estimation in perturbed areas. Conference on Decision and Control; , 2007.
- 342 19. Vissière, D.; Martin, A.; Petit, N. Using magnetic disturbances to improve IMU-based position estimation.
343 European Control Conference; , 2007; pp. 2853–2858.
- 344 20. Chesneau, C.I.; Hillion, M.; Hullo, J.F.; Thibault, G.; Prieur, C. Improving magneto-inertial attitude
345 and position estimation by means of a magnetic heading observer. International Conference on Indoor
346 Positioning and Indoor Navigation (IPIN); , 2017; pp. 1–8.
- 347 21. Dorveaux, E.; Boudot, T.; Hillion, M.; Petit, N. Combining inertial measurements and distributed
348 magnetometry for motion estimation. American Control Conference; , 2011; pp. 4249–4256.
- 349 22. Zampella, F.J.; Jiménez, A.R.; Seco, F.; Prieto, J.C.; Guevara, J.I. Simulation of Foot-Mounted IMU Signals for
350 the Evaluation of PDR Algorithms. International Conference on Indoor Positioning and Indoor Navigation
351 (IPIN); , 2010; pp. 1–6.
- 352 23. Kuipers, J. *Quaternions and rotation sequences*; 1999.
- 353 24. Zmitri, M.; Fourati, H.; Prieur, C. Improving Inertial Velocity Estimation Through Magnetic Field
354 Gradient-based Extended Kalman Filter. International Conference on Indoor Positioning and Indoor
355 Navigation (IPIN); , 2019.

- 356 25. Madgwick, S.O.; Harrison, A.J.; Vaidyanathan, R. Estimation of IMU and MARG orientation using a
357 gradient descent algorithm. *International Conference on Rehabilitation Robotics*; , 2011; pp. 1–7.
- 358 26. Süli, E. *Numerical Solution of Ordinary Differential Equations*; 2010.
- 359 27. Choukroun, D.; Bar-Itzhack, I.Y.; Oshman, Y. A Novel Quaternion Kalman Filter. *IEEE Transactions on*
360 *Aerospace and Electronic Systems* **2006**, *24*, 174–190.
- 361 28. Renaudin, V.; Combettes, C. Magnetic, acceleration fields and gyroscope quaternion (MAGYQ)-based
362 attitude estimation with smartphone sensors for indoor pedestrian navigation. *IEEE Transactions on*
363 *Aerospace and Electronic Systems* **2014**, *14*, 22864–22890.
- 364 29. Mahony, R.; Hamel, T.; Pflimlin, J.M. Nonlinear complementary filters on the special orthogonal group.
365 *IEEE Transactions on Automatic Control* **2008**, *53*, 1203–1218.
- 366 30. Wu, J.; Zhou, Z.; Fourati, H.; Li, R.; Liu, M. Generalized Linear Quaternion Complementary Filter for
367 Attitude Estimation from Multi-Sensor Observations: An Optimization Approach. *IEEE Transactions on*
368 *Automation Science and Engineering* **2019**, *16*, 1330–1343.
- 369 31. Martin, P.; Salaun, E. Design and implementation of a low-cost observer-based attitude and heading
370 reference system. *Control Engineering Practice* **2010**, *18*, 712–722.
- 371 32. Ming, M.; Song, Q.; Gu, Y.; Li, Y.; Zhou, Z. An Adaptive Zero Velocity Detection Algorithm Based on
372 Multi-Sensor Fusion for a Pedestrian Navigation System. *Sensors* **2018**, *18*, 3261.
- 373 33. Skog, I.; Händel, P.; Nilsson, J.O.; Rantakokko, J. Zero-Velocity Detection—An Algorithm Evaluation. *IEEE*
374 *Transactions on Biomedical Engineering* **2010**, *57*, 2657–2666.
- 375 34. Xsens MTi Products. <https://www.xsens.com/mti-products>. Accessed: 2020-07-21.
- 376 35. Oppenheim, A.V.; Verghese, G.C. *Signals, Systems and Inference*; 2015.